Available online at www.sciencedirect.com

ScienceDirect

Advances in Space Research xxx (2020) xxx–xxx

ADVANCES IN SPACE RESEARCH (a COSPAR publication)

www.elsevier.com/locate/asr

GPS III Vespucci: Results of half a year in orbit

Peter Steigenberger [a,*], Steffen Thoelert [b], Oliver Montenbruck [a]

[a] Deutsches Zentrum für Luft- und Raumfahrt (DLR), German Space Operations Center (GSOC), Münchener Straße 20, 82234 Weßling, Germany
[b] Deutsches Zentrum für Luft- und Raumfahrt (DLR), Institute for Communications and Navigation (IKN), Münchener Straße 20, 82234 Weßling, Germany

Received 13 December 2019; received in revised form 15 March 2020; accepted 19 March 2020

Abstract

The spacecraft nicknamed Vespucci is the first GPS III satellite launched in December 2018. Numerous receivers of the global International GNSS Service network tracked the signals of this new generation of GPS spacecraft from January to July 2019. This data set serves as the basis for analysis of broadcast ephemeris performance and clock stability, as well as solar radiation pressure and satellite antenna phase center models. Different empirical orbit models are tested, and box-wing models are developed based on approximate dimensions, mass, and assumed optical properties. The box-wing models show in general a better performance than the empirical models. Compared to Block IIF satellites, the stability of the GPS III rubidium clock is higher for integration times up to 10 s. At longer integration times, the stability of both clocks is similar but the GPS III clock does not suffer from frequency-specific line bias variations that affect the apparent IIF clock. Estimated antenna phase center offsets agree on the centimeter level with the calibrations published by the manufacturer. Measurements with a 30-m high-gain antenna revealed that the satellite did not stop signal transmission in July 2019 but switched to non-standard codes and codes beyond the tracking capabilities of commercial GNSS receivers. Prior to this hibernation mode, a 70 days test without broadcast ephemeris update was conducted during which the user range error increased to roughly 1 km.

Keywords: GNSS; Global Positioning System; GPS III; solar radiation pressure modeling; box-wing model; satellite antenna phase center offsets

1. Introduction

The first GPS III spacecraft is named after the Italian explorer Amerigo Vespucci. It was launched on December 23, 2018, from Cape Canaveral with a Falcon-9 rocket. The satellite is also denoted by its space vehicle number (SVN) as GPS-74. In contrast to the previous generation of Block IIF satellites with Boeing as prime contractor, the GPS III spacecraft are manufactured by Lockheed Martin, which already built the Block IIR and IIR-M satellites. A general overview of the GPS III satellite and its payload can be found in Marquis and Shaw (2011).

Table 1 gives an overview of basic properties of the different generations (blocks) of GPS satellites. From generation to generation, the size of the satellite bus, its mass and power, as well as the transmit power of the navigation signals increased. The GPS III launch mass is 3681 kg (Alexander and Martin, 2018) but the on-orbit mass of 2161 kg is significantly lower due to the fuel consumption for bringing the satellite from its transfer orbit to the designated orbit. The size of the spacecraft body is 2.46 m × 1.78 m × 3.40 m.

The GPS III spacecraft are equipped with three Rubidium atomic frequency standard (RAFS) clocks based on the RAFSs already flown on GPS Block IIR and IIR-M (Wu and Feess, 2000). Following Cameron (2019), GPS III satellites provide

* Corresponding author.
E-mail addresses: peter.steigenberger@dlr.de (P. Steigenberger), steffen.thoelert@dlr.de (S. Thoelert), oliver.montenbruck@dlr.de (O. Montenbruck).

https://doi.org/10.1016/j.asr.2020.03.026
0273-1177/

Please cite this article as: P. Steigenberger, S. Thoelert and O. Montenbruck, GPS III Vespucci: Results of half a year in orbit, Advances in Space Research, https://doi.org/10.1016/j.asr.2020.03.026

Table 1
Basic properties of different GPS block types according to Alexander and Martin (2018); Hegarty (2017); Rodriguez Solano (2014) U.S. Air Force (2015); Steigenberger et al. (2018). Values in brackets are based on assumptions.

	Block I	Block II/IIA	Block IIR/IIR-M	Block IIF	Block III
1st launch	Feb 1978	Feb 1989	Jul 1997	May 2010	Dec 2018
Mass	455 kg	843 kg/930 kg	1080 kg	1633 kg	2161 kg [b]
Body size [m]	1.3 × 1.2 × 1.8	1.9 × 1.5 × 1.8	2.1 × 2.0 × 2.1	2.5 × 2.1 × 1.8	1.8 × 2.5 × 3.4
Span width	5.3 m	5.3 m	11.4 m	17.5 m	15 m
Power	400 W	700 W	1140 W	1952 W [a]	4480 W [a]
Transmit power	(50 W)	50 W	60 W/145 W	240 W	(300 W)

[a] End of life.
[b] In-orbit mass according to Alexander and Martin (2018). Solar radiation pressure estimates indicate a higher mass, see Section 4.

– three times better positioning accuracy compared to Block IIF with a 1 m user range error at 24 h
– improved anti-jamming capability
– the additional civil L1C signal (Betz et al., 2007)
– the 2nd generation civil navigation message CNAV-2
– a design life time of 15 years, three more years compared to Block IIF.

For operation of the GPS III satellites, the next generation operational control system (OCX) is required. The current OCX Block 0 version has basic capabilities for launch and checkout but there are several limitations until Block 1 delivery which is expected in June 2021 (Erwin, 2019). As a remedy, the Contingency Operations Program (COps) was put in place and enabled a renewed operation of GPS-74 from October 2019 onwards (GPS World, 2019).

GPS-74 is a new type of satellite, that is not yet fully characterized by the scientific GNSS user community. Therefore, a focus of the present study is to contribute to an improved modeling of the satellite as a basis for highly accurate orbit and clock products. In particular, the limited availability of satellite metadata poses a challenge for precise orbit determination based on physical models. Comprehensive satellite metadata like attitude law, geometry and optical properties of the satellite surfaces are presently published by the providers of the European system Galileo (GSA, 2017) as well as the Japanese regional Quasi-Zenith Satellite System (QZSS, Cabinet Office, 2019). Metadata for GPS III are currently limited to approximate mass and body dimensions (Alexander and Martin, 2018) as well as satellite antenna phase center offsets (PCOs) and inter-signal correction parameters (Lockheed Martin, 2019b). The optical properties of the satellite surfaces that are required for solar radiation pressure modeling are currently not publicly available. In addition, it is not clear if the dimensions of the satellite body given in Alexander and Martin (2018) refer to the solid box of the satellite or if they refer to an envelope including, e.g., the antenna panel. Therefore, several assumptions have to be made for the development of a GPS III box-wing model and its empirical tuning.

The present study is based on GPS-74 observations collected between January and July 2019. Section 2 discusses the transmission of navigation signals with standard and non-standard codes as well as the navigation message. The models and parameters applied for precise orbit determination are introduced in Section 3. Empirical and physical approaches for solar radiation pressure modeling are detailed in Section 4. The quality of the estimated orbit and clock parameters is assessed in Sections 5 and 6. Finally, the published satellite antenna PCO calibration values are validated with parameters estimated from GPS observations in Section 7.

2. Signal transmission and broadcast ephemerides

First navigation signals of GPS-74 were received roughly two weeks after the launch. A detailed GPS III signal analysis based on high-gain antenna as well as receiver measurements is given in Thoelert et al. (2019). The following sections focus on transmission of non-standard signals after mid of July 2019 and a long-term propagation test of the broadcast ephemerides starting in May 2019.

2.1. Navigation signals

The transmission of standard navigation signals started on January 9, 2019 at 00:01 UTC with pseudo random noise (PRN) number G04. A transmission outage occurred between March 19, 22:11 UTC and March 20, 19:46 UTC. Signal transmission with PRN G04 stopped on July 12, 2019. According to Cozzens (2019), the on-orbit checkout and test activities were officially completed on that date. PRN G04 was subsequently reassigned to the old Block IIA satellite GPS-36 on 18 July 2019. During the total six months of signal transmission, the health status of GPS-74 was set to unhealthy.

Measurements with a 30-m high-gain antenna operated by the German Aerospace Center (DLR) in Weilheim (Germany) revealed that GPS-74 continued to transmit navigation signals after mid July, even though the signals could no longer be tracked by common receivers. L1 spectra before and after this transition are shown in Fig. 1. Aside from a 10 to 15 dB drop in the overall power, distinct changes in the spectral characteristics occurred after 12 July. In particular, a pronounced dip at the L1 center frequency (1575.42 MHz) may be noted, which comes along

Please cite this article as: P. Steigenberger, S. Thoelert and O. Montenbruck, GPS III Vespucci: Results of half a year in orbit, Advances in Space Research, https://doi.org/10.1016/j.asr.2020.03.026

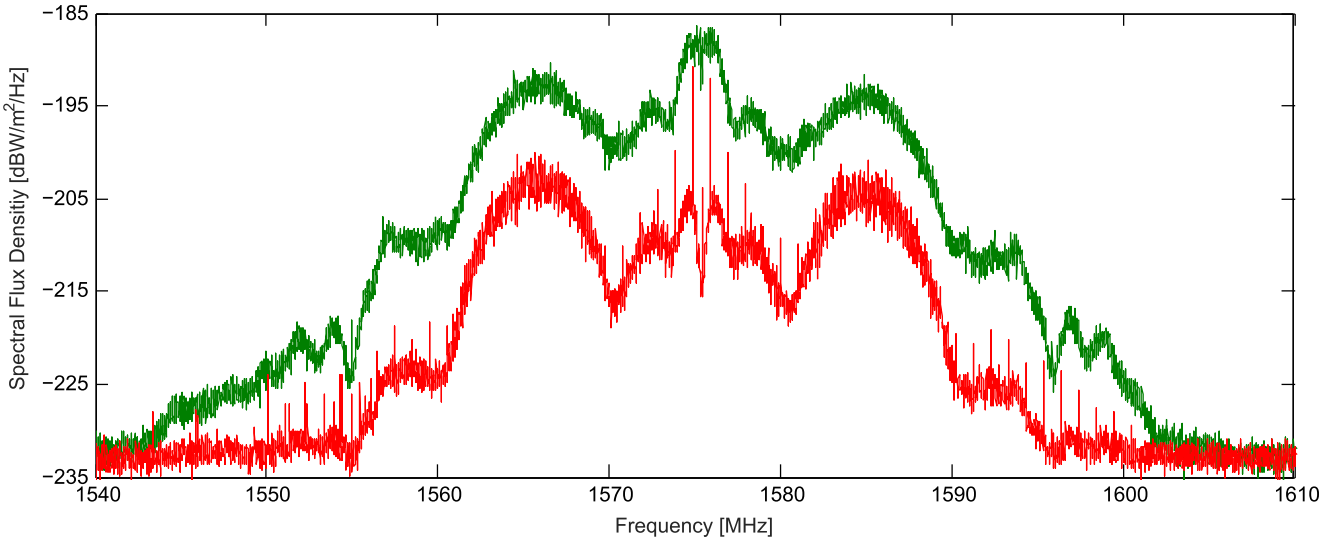

Fig. 1. L1 spectral flux density of GPS-74 measured with the 30-m high-gain antenna. The green curve was recorded on January 15, 2019 and refers to nominal signal transmission. The red curve was recorded on July 17, 2019, when the spacecraft transmitted with reduced signal power and used non-standard C/A codes. (For interpretation of the references to colour in this figure legend, the reader is referred to the web version of this article.)

with a narrow line spectrum at a spacing of 1.023 MHz. Both features are related to the replacement of the L1 C/A code modulation by a non-standard code (NSC; see IS-GPS-200K, 2019) made up of an alternating sequence of +1 and −1 chips.

Other than for the L1 C/A component, the L1C channel appears to be modulated with a regular ranging code during the "hibernation" of GPS-74 from mid July to October 2019. Using a software receiver and radio-frequency samples collected with the 30-m antenna, a high correlation was obtained for the PRN 117 code sequence from a Weil Code generator in combination with the Weil Index and Insertion Index provided in Table 3.2-2 of IS-GPS-800F (2019). Even though the L1C signal ICD defines PRN numbers up to 210, codes for high PRNs were not supported by geodetic GPS receivers in this time frame. Overall, the modified signal transmission caused a 3-month outage in the IGS tracking coverage of GPS-74. M-code and P(Y)-code signals are present on L1 and L2 but with significantly reduced power level. The total power differences per band are −12 dB, −4.5 dB, and −9 dB for L1, L2, and L5, respectively.

Since October 10, 2019, G04/GPS-74 is included in the almanac, and normal signal transmissions of GPS-74 with PRN G04 restarted on October 21. At 20:05 UTC, the L1 C/A, L1 P(Y), and L2 P(Y) signals were activated, L1C, L2C, and L5 followed at 22:08 UTC. GPS World (2019) reports that the GPS III Contingency Operations Program (COps) successfully connected to GPS-74 on that date. COps allows for operation of the GPS III satellites together with the legacy satellites before completion of OCX Block 1.

2.2. Broadcast ephemerides

The transmission of broadcast ephemerides started simultaneously with the navigation signal transmission on January 9, 2019. GPS-74 transmits the legacy navigation message (LNAV) on L1 C/A, the civil navigation message (CNAV) as part of the L2C and L5 signals, and the 2nd generation CNAV-2 on the L1C signal. During the first six months of operation, the CNAV-2 messages provided essentially the same parameter set as CNAV on L2 and L5, but added distinct inter-signal corrections (ISCs) for the pilot and data component of the L1C signal. With an average value of 2.8 m for April 2019, the signal-in-space range error (SISRE) of GPS-74 is worse by a factor of up to five compared to IIF satellites with Rubidium clocks. This can mainly be related to an extended upload interval of typically four days as opposed to one day for the rest of the constellation. Evidently the apparent performance degradation is related to the non-operational status of GPS-74 and does not indicate the expected performance once the satellite is declared healthy. Only negligible differences may be noted between SISRE values for LNAV, CNAV, and CNAV-2, since all messages are presently derived from the same source of orbit and clock prediction and uploaded only once per day. As such, the improved smoothness of the CNAV/CNAV-2 ephemeris and the availability of ISCs for users of the open L1 signals (C/A or L1C) can only partly be materialized by civil navigation users.

CNAV and CNAV-2 include several indices that allow to compute the "non-elevation dependent integrity assured user range accuracy" ($IAURA_{NED}$, IS-GPS-200K, 2019). Between May 7 and July 8, 2019, the "data sequence propagation time" of CNAV that represents the epoch of the latest observation data entering the orbit and clock prediction didn't change for GPS-74. The resulting degradation of $IAURA_{NED}$ is illustrated in Fig. 2. Within two months, $IAURA_{NED}$ gradually degraded to up to 1400 m. During normal operations, $IAURA_{NED}$ values are usually within one to seven meters.

Please cite this article as: P. Steigenberger, S. Thoelert and O. Montenbruck, GPS III Vespucci: Results of half a year in orbit, Advances in Space Research, https://doi.org/10.1016/j.asr.2020.03.026

Figure 2 also shows the signal-in-space range error at the worst user location ($SISRE_{WUL}$, Montenbruck et al., 2015b) computed from differences between broadcast ephemerides and the precise orbit and clock product discussed in Section 3. The radial and cross-track orbit differences are within ± 10 m whereas the along-track differences reach up to 600 m. The resulting $SISRE_{WUL}$ shows once per revolution periodic variations and has a maximum of 600 m. However, $SISRE_{WUL}$ values are always well below $IAURA_{NED}$ that provides the upper bound for the accuracy of the broadcast ephemerides.

3. Orbit determination

Despite being marked as "unhealthy" and despite not being part of the almanac, GPS-74 was already tracked by a substantial number of stations of the International GNSS Service (IGS, Johnston et al., 2017). For the present study, a subset of 156 IGS tracking stations was selected to estimate GPS orbit and clock parameters. However, only 71 of those stations were able to track GPS-74 (see Fig. 3), as certain receiver types do not support tracking of satellites that are not included in the almanac. While this is less than half of the total number of stations, it is fully sufficient to perform precise orbit and clock determination of the new GPS III satellite. The GPS data were processed with the NAPEOS software (Springer, 2009) using daily batches and a 5 min observation sampling. The analysis interval covers the full first transmission period of GPS-74 from January 9 until July 12, 2019 (day of year 9–193/2019). Details on the GPS data modeling and the estimated parameters are given in Table 2.

Solar radiation pressure modeling, satellite antenna phase center modeling, and phase windup modeling all rely on a consistent definition of spacecraft body axis and the inertial attitude of the spacecraft. Axis conventions for

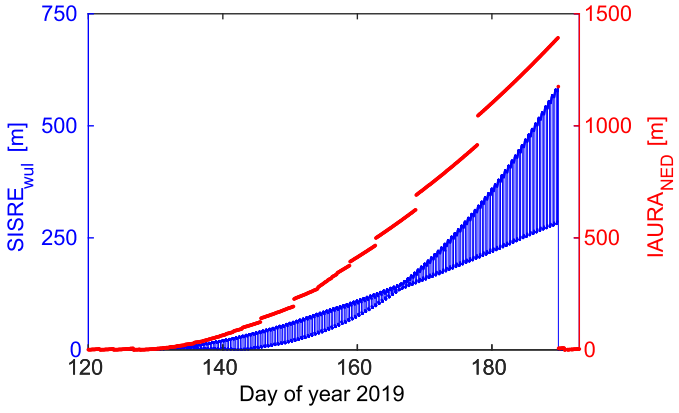

Fig. 2. Signal-in-space range error at the worst user location ($SISRE_{WUL}$, blue) and non-elevation dependent integrity assured user range accuracy ($IAURA_{NED}$, red) of GPS-74. (For interpretation of the references to colour in this figure legend, the reader is referred to the web version of this article.)

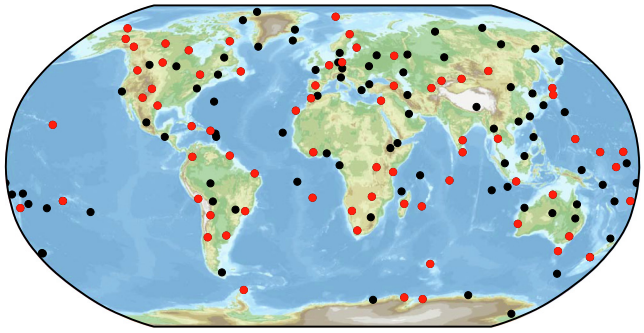

Fig. 3. GPS tracking stations used for precise orbit and clock determination. Stations tracking GPS-74 are given in red. (For interpretation of the references to colour in this figure legend, the reader is referred to the web version of this article.)

GPS III established by the manufacturer are defined in Marquis and Shaw (2011). The +Z surface carries the L-band transmit antenna array and the ±Y axis coincides with the rotation axis of the solar panels. Individual axes in the manufacturer frame may be distinguished by the prominent sunshade of the optical sensor of the burst detector which is located in the +X/+Y corner of the +Z surface.

With respect to spacecraft attitude, the GPS III satellites employ a continuous yaw steering, which nominally keeps the Y-axis perpendicular to the Sun-spacecraft-Earth plane. While official specifications are presently missing, it appears plausible to assume that GPS III applies the same conventions as the Block IIR satellites built by the same manufacturer. Here, the −X panel is permanently sunlit while the opposite +X panel always points to deep space (Montenbruck et al., 2015a). This assumption is further supported by the inspection of images of the second GPS III spacecraft taken shortly before launch (Lockheed Martin, 2019a). These show that the +X panel is covered by black multi-layer insulation (MLI), whereas a silver MLI is used on the −X panel. Since the latter provides a higher reflectivity, it appears better suited for the Sun-exposed surface, and suggests again that the −X panel points towards the Sun. Finally, the assumed assignment of the individual body axes is also supported by the estimation of transmit antenna phase center offsets as discussed in Section 7. Here, a better consistency with manufacturer calibrations (Lockheed Martin, 2019b) is achieved when assuming that the −X panel, rather than the +X panel, is permanently sunlit.

As discussed in Montenbruck et al. (2015a), the IGS favors a harmonized body axis convention for all yaw-steering GNSS satellites in which the Sun-pointing body axis is designated as $+X_{IGS}$. Similar to the IIR satellites, this implies opposite signs for the X and Y coordinates of GPS III when referred to IGS versus manufacturer conventions. Unless otherwise noted, all specifications of coordinates and axes in the remainder of this study will refer to IGS conventions.

Please cite this article as: P. Steigenberger, S. Thoelert and O. Montenbruck, GPS III Vespucci: Results of half a year in orbit, Advances in Space Research, https://doi.org/10.1016/j.asr.2020.03.026

Table 2
Selected modeling options and estimation parameters of the GPS data processing.

Basic observables	GPS L1 C/A and L2 P(Y) code and phase observations
Sampling	5 min for standard solutions, 30 s for high-rate clock solution
Antenna model	igs14.atx for receiver and satellite antennas (Rebischung and Schmid, 2016)
Earth radiation pressure	Springer (2009) for empirical models, monthly CERES maps (Wielicki et al., 1996) for box-wing model
Antenna thrust	Steigenberger et al. (2018, 2019)
Station coordinates	estimated every day
Ambiguities	fixed to integers for baselines up to 6000 km with the Melbourne Wübbena approach (Melbourne, 1985; Wübbena, 1985)
Receiver clocks	estimated epoch-wise
Satellite clocks	estimated epoch-wise
Troposphere zenith delays	2 h, a priori from Boehm et al. (2007) and Saastamoinen (1972), Global Mapping Function (Boehm et al., 2006)
Earth rotation	x-/y-pole + rates, LOD estimated every day, UT1 heavily constrained to USNO final EOP series
Satellite orbits	state vector + SRP according to Table 4 along-track constant, sine, cosine once per revolution accelerations, constrained with 0.1 nm/s^2

The nominal yaw-steering attitude is applied by GPS III satellites for most of the year but cannot be exactly fulfilled during periods of low Sun elevation above the orbital plane. Here, excessive yaw rates would be required near orbit noon and midnight to keep the solar panel rotation axis strictly perpendicular to the Sun and Earth direction. A rate-limited yaw steering must therefore be applied in these periods but details of this specific mode have not yet been publicly disclosed. Unfortunately, it is not possible to determine the attitude behavior with the reverse PPP technique as it was done by Dilssner (2010) for the Block IIF satellites, since the horizontal antenna offsets are close to zero. In the absence of other information, the Block IIR attitude law (Kouba, 2009) for noon- and midnight-turns during the eclipse season is also used for the GPS III satellite within our study. This choice is mainly motivated by the fact that both types of satellites were designed by the same manufacturer but needs to be checked against observations. Even though a final confirmation is lacking, use of this model for phase-windup modeling did not result in discontinuities or variations of estimated clock offsets near noon and midnight beyond the statistical clock variations observed in other periods.

In contrast to GLONASS, Galileo, and BeiDou, and future Block IIIF spacecraft, the first generation of GPS III satellites is not equipped with retro-reflector arrays for satellite laser ranging (SLR) that allow for external accuracy assessment of GNSS satellite orbits (Sosnica et al., 2015). Therefore, the following quantities are used to assess the GPS-74 orbit quality (e.g., Steigenberger et al., 2015):

Estimated SRP parameters:
if the a priori model covers all important features of the satellite, the estimated empirical SRP parameters should not show systematic effects or biases.

Day-boundary discontinuities:
3D distance between the orbital positions obtained from two consecutive days at the midnight epoch.

2-day orbit fits:
based on two individual and independent 1-day orbit arcs, a 2-day arc is fitted with the same orbit model as for the original arcs. The RMS of the original 1-day orbits w.r.t. the newly determined 2-day arc is used as quality indicator.

Orbit predictions:
RMS of one-day orbit prediction w.r.t. the orbit of the next day based on observations.

Clock residuals:
standard deviation (STD) of clock residuals after removing a 2nd order polynomial per daily solution.

Actual results and a performance characterization of GPS-74 orbit determination will be presented in Sections 5 and 6 after discussing the modeling of solar radiation pressure for this spacecraft.

4. Solar radiation pressure modeling

Accurate modeling of the solar radiation pressure (SRP) forces acting on a GNSS satellite is a prerequisite for precise orbit determination. Two major categories for SRP modeling can be distinguished. Empirical models do not require knowledge about the satellite and consider the SRP by estimating empirical parameters. Widely used empirical models are the empirical CODE orbit model (ECOM-2, Arnold et al., 2015) developed at the Center for Orbit Determination in Europe (CODE) and the GPS Solar radiation Pressure Model developed at the Jet Propulsion Laboratory (GSPM, Sibthorpe et al., 2011).

Please cite this article as: P. Steigenberger, S. Thoelert and O. Montenbruck, GPS III Vespucci: Results of half a year in orbit, Advances in Space Research, https://doi.org/10.1016/j.asr.2020.03.026

The ECOM-2 used in this paper models the SRP in a Sun-oriented reference frame with axes D pointing towards the Sun, Y along the satellite's solar panel axis and B completing a right handed system. In each direction, constant and optionally periodic terms are used to describe the acceleration

$$\begin{aligned} a_{\mathrm{D}} &= \mathrm{D}_0 + \mathrm{D}_{2\mathrm{C}} \cdot \cos 2\Delta u + \mathrm{D}_{2\mathrm{S}} \cdot \sin 2\Delta u \\ a_{\mathrm{Y}} &= \mathrm{Y}_0 \\ a_{\mathrm{B}} &= \mathrm{B}_0 + \mathrm{B}_{\mathrm{C}} \cdot \cos \Delta u + \mathrm{B}_{\mathrm{S}} \cdot \sin \Delta u \end{aligned} \quad (1)$$

with estimated parameters D_0, $\mathrm{D}_{2\mathrm{C}}$, $\mathrm{D}_{2\mathrm{S}}$, Y_0, B_0, B_{C}, B_{S}. Δu denotes the argument of latitude of the satellite relative to the argument of latitude of the Sun in the orbital plane. ECOM-2 in general allows for an arbitrary number of harmonic coefficients but the coefficients shown in Eq. 1 represent the maximum number used in this paper. The older ECOM-1 model (Beutler et al., 1994) does not include the 2nd order terms in D direction that are important for a proper modeling of stretched satellite bodies like those of the Galileo satellites (Prange et al., 2017).

Physical models, on the other hand, consider the dimensions, mass and optical properties of the satellite. Accelerations acting on individual surfaces of the satellite are computed based on absorption, diffuse, and specular reflection of the incoming photons. Corresponding coefficients α, δ, and ρ describe the optical properties of the surface elements. A simple approach for physical modeling is the so-called box-wing model where the satellite body is represented by a cuboid (box) and the solar panels by rectangular surfaces (wings). Several such models have been developed for different kinds of GNSS satellites (Bury et al., 2019; Duan et al., 2019; Montenbruck et al., 2017; Rodriguez-Solano et al., 2012; Zhao et al., 2018). With more detailed knowledge about the structure of the satellite, a ray-tracing approach can be used (Bhattarai et al., 2019; Darugna et al., 2018; Li et al., 2018).

The acceleration for a box surface i of the satellite body due to solar radiation pressure assuming instantaneous diffuse thermal reradiation of the absorbed radiation (Montenbruck et al., 2015c) is

$$\begin{aligned} a_{box,i} = \; & -P \cdot \frac{A_i}{m} \cdot \cos\theta_i \\ & \left[(\alpha_i + \delta_i) \cdot \left(\mathbf{e}_\odot + \tfrac{2}{3}\mathbf{e}_{n,i} \right) + 2\rho_i \cos\theta_i \cdot \mathbf{e}_{n,i} \right] \end{aligned} \quad (2)$$

where A_i is the area of surface i, θ_i is the angle between the surface normal $\mathbf{e}_{n,i}$ and the Sun direction $\mathbf{e}_\odot$, and m is the satellite mass. The solar radiation pressure at satellite position $\mathbf{r}$ is given by

$$P \approx \frac{1367\ \mathrm{W/m^2}}{c} \cdot \left(\frac{1\ \mathrm{AU}}{\mathbf{r}_\odot - \mathbf{r}} \right)^2 \quad (3)$$

where c stands for the vacuum speed of light. For nominal attitude (Montenbruck et al., 2015a), only the surfaces $i = +\mathrm{Z}, -\mathrm{Z}, +\mathrm{X}$ are lit by sunlight.

For the solar panels it is assumed that thermal reradiation of the front and back side are identical (introducing no net acceleration) and that they are always pointed towards the Sun:

$$\begin{aligned} a_{sp} = \; & -P \cdot \frac{A_{sp}}{m} \\ & \left[(\alpha_{sp} + \delta_{sp}) \cdot \mathbf{e}_\odot + \tfrac{2}{3}\delta_{sp} \cdot \mathbf{e}_{n,sp} + 2\rho_{sp} \cos\theta_{sp} \cdot \mathbf{e}_{n,sp} \right] \end{aligned} \quad (4)$$

For precise orbit determination, the box-wing models presented below are not used as stand-alone models but combined with a 5-parameter ECOM-1 model. By estimating the empirical D_0, Y_0, B_0, B_{C}, and B_{S} terms, residual modeling deficiencies due to uncertainties of areas and optical properties, the detailed body structure, as well as shading effects can partly be compensated.

Overall, two different box-wing models are considered in this study, which differ in the assumed body-dimensions (Table 3). BW-1 describes a stretched satellite body in accord with geometric properties and dimensions of a spacecraft model shown in Fig. 4. As discussed in the subsequent sections, use of the BW-1 a priori box-wing model minimizes seasonal variations in the estimated empirical SRP parameters but shows distinct orbit-periodic variations of the estimated clock offset. As an alternative, the BW-2 model is therefore considered. It describes an almost cubic spacecraft body, which apparently contradicts the actual shape. The respective cross-sections have been adjusted such as to minimize the orbit periodic clock variations at the expense of showing more pronounced seasonal variations of the empirical SRP parameters. Other than for Galileo (Montenbruck et al., 2015c), no simultaneous minimization of the D_0 and clock variations could be achieved for GPS-74 using a simple box-wing a priori SRP model. A detailed discussion of these aspects and comparison of both models is provided in Section 5.

The surface characteristics for the box-wing model were obtained from images of the second GPS III spacecraft shortly before launch (Lockheed Martin, 2019a). These images show that the ±X and +Z surfaces are covered by multi-layer insulation (MLI). For the +Z surface that carries the L-band transmit antenna array, silver, radio-transparent MLI is used. In contrast to Fig. 4, the complete −X surface (including the golden oxidizer tank in Fig. 4) is covered by black MLI, whereas the +X surface is basically covered by silver MLI. For the −Z surface, the optical properties of black MLI are adopted, as parts of the sur-

Table 3
Areas and optical properties for the two GPS III box-wing models (BW-1, BW-2) considered in this study. A satellite mass of 2600 kg is adopted in both models.

Surface	Area [m²]		α_i	δ_i	ρ_i
	BW-1	BW-2			
+Z bus	4.0	6.0	0.44	0.46	0.10
−Z bus	4.0	6.0	0.94	0.06	0.00
+X bus	7.5	5.7	0.44	0.46	0.10
Solar panels	28.2		0.92	0.00	0.08

Please cite this article as: P. Steigenberger, S. Thoelert and O. Montenbruck, GPS III Vespucci: Results of half a year in orbit, Advances in Space Research, https://doi.org/10.1016/j.asr.2020.03.026

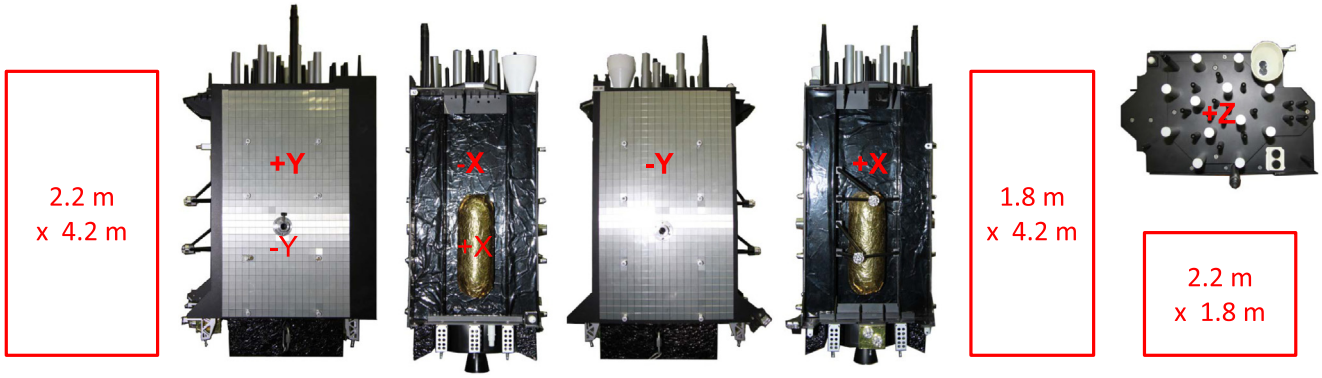

Fig. 4. GPS-74 satellite surfaces according to IGS axes conventions obtained from a scale model by the manufacturer. The red boxes represent the dimensions used for box-wing model BW-1. (For interpretation of the references to colour in this figure legend, the reader is referred to the web version of this article.)

face are covered by this type of MLI whereas the optical properties of the launch adapter are completely unknown.

Optical properties of the two different types of MLI are taken from Montenbruck et al. (2017) and listed in Table 3. For the solar panels, the optical properties of the Block IIR satellites (Fliegel and Gallini, 1996) resulted in a significantly too high SRP acceleration. Therefore, the optical properties of Galileo (GSA, 2017) are used, with a higher absorption and a lower reflectivity resulting in a lower acceleration.

Figure 5 illustrates the estimated direct solar radiation parameter D_0 for all GPS satellites active during the analysis interval. ECOM-1 has been used and no a priori box-wing model has been applied. D_0 is proportional to the effective area in Sun direction and inversely proportional to the satellite mass. The four different satellite blocks are clearly discernible due to their significantly different mean values. Variations in D_0 are largely related to variations of the effective area of the satellite in Sun direction. The highest dispersion is visible for Block IIR satellites in orbital plane E (GPS-47, -50, -51) and F (GPS-41, -43, -55, -60), which show the largest variations of the elevation of the Sun above the orbital plane. For Block IIF, D_0 variations are less pronounced due to the higher mass and a reduced stretching of the satellite body.

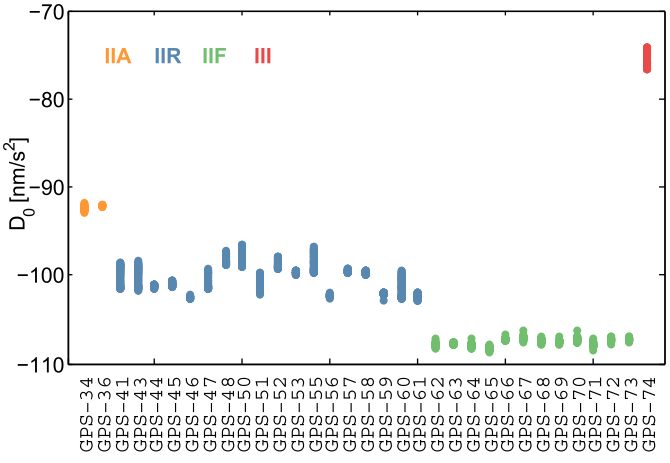

Fig. 5. Estimated direct solar radiation pressure coefficient D_0. (For interpretation of the references to colour in this figure legend, the reader is referred to the web version of this article.)

The D_0 estimates of GPS-74 show a mean value of $-75.5\ \mathrm{nm/s^2}$, which is about 30% smaller than for Block IIF and 25% smaller than for Block II-R. However, the estimated D_0 values appear incompatible with the GPS-74 in-orbit mass of 2161 kg given in Alexander and Martin (2018). Tests with this mass and an initial box-wing model resulted in D_0 residual estimates of about $28\ \mathrm{nm/s^2}$. A revised mass of 2600 kg has therefore been adopted for this study. The discrepancy between the "observed" and published mass suggests that Alexander and Martin (2018) refer to a "dry mass" and do not account for remaining fuel at the begin of in-orbit operations.

5. Orbit analysis

To assess the quality of the box-wing and empirical SRP models in more detail, four solutions with different SRP modeling approaches are computed, see Table 4. The orbit quality is assessed with the methods described in Section 3. Figure 6 shows the estimated SRP parameters D_0 and B_C as a function of the Sun elevation β above the orbital plane. Compared to a standalone ECOM-1 model, use of the BW-1 a priori model reduces the standard deviation of the estimated D_0 parameters from $0.8\ \mathrm{nm/s^2}$ to $0.3\ \mathrm{nm/s^2}$. ECOM-2 and BW-2 + ECOM-1 have significantly higher D_0 variations of $1.3\ \mathrm{nm/s^2}$ and $1.4\ \mathrm{nm/s^2}$, respectively. All solutions show a slight asymmetry in D_0 estimates w.r.t.

Table 4
Options for solar radiation pressure modeling. For each ID, the estimated parameters and optional a priori box wing models are marked. D_2 stands for the parameters D_{2C} and D_{2S} and B_1 for the parameters B_C and B_S in Eq. (1).

ID	D_0	Y_0	B_0	D_2	B_1	BW v1	BW v2
ECOM-1	×	×	×		×		
ECOM-2	×	×	×	×	×		
BW-1	×	×	×		×	×	
BW-2	×	×	×		×		×

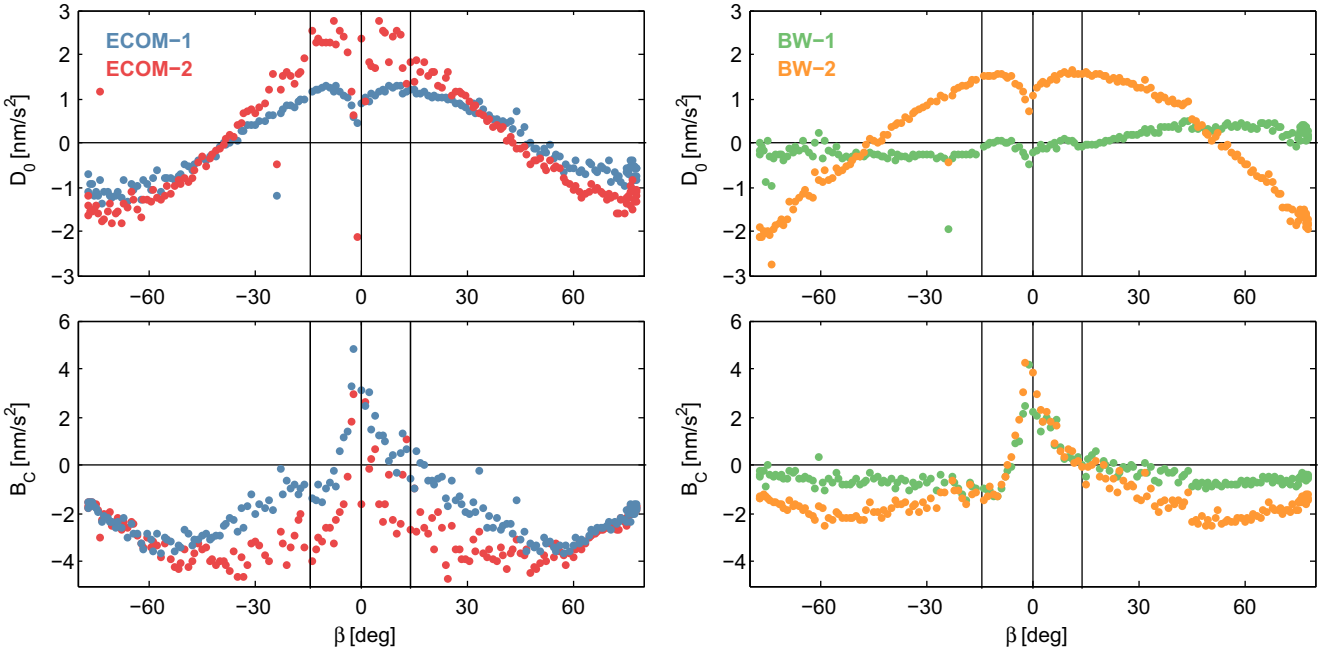

Fig. 6. Solar radiation pressure coefficients D_0 and B_C versus elevation of the Sun above the orbital plane. For D_0, the mean value of each solution is subtracted. ECOM-1: −75.5 nm/s^2, ECOM-2: −75.0 nm/s^2, BW-1: 0.1 nm/s^2, BW-2: −2.7 nm/s^2. (For interpretation of the references to colour in this figure legend, the reader is referred to the web version of this article.)

positive and negative β-angles. The reason for this behavior is unknown but may be related to asymmetries of the spacecraft structure that cannot be addressed by the considered SRP models, or deviations from the Block IIR attitude assumed in our processing.

For the B_C parameters, ECOM-1 and ECOM-2 are almost identical for $|\beta| > 60°$ and also the STD of 1.7 nm/s^2 matches for both solutions. Compared to the purely empirical ECOM-1 or -2 models, the B_C estimates are closer to zero and have smaller STDs of 1.1 and 1.5 nm/s^2 when using the BW-1 or BW-2 a priori models. The other ECOM parameters do not change significantly if an a priori box-wing model is applied.

The residuals of the estimated clock offsets after detrending with a second order polynomial over the daily data arcs are given in Fig. 7. ECOM-1 introduces a small dependency on the Earth-satellite-Sun angle ϵ. This dependency is more pronounced for ECOM-2 resulting in an increase of 45% of the clock residual STD listed in Table 5. The BW-1 clock residuals show a smaller variation with ϵ than for ECOM-2 but a larger variation than obtained with the standalone ECOM-1 model. The BW-2 a priori model, which has been specifically designed to minimize orbit-periodic clock variations, achieves a STD of 2.8 cm which is the smallest of all solutions.

Further orbit quality measures are listed in Table 5. With RMS residuals of 1.4 cm, the best 2-day orbit fit performance is achieved when using the BW-1 SRP model, even though results for other models are only marginally worse. For the 1-day orbit predictions, differences between the solutions are at the 2 cm level or about 10% of the actual prediction errors. Here, ECOM-2 performs better than ECOM-1 but the BW-1 model again achieves the lowest errors. The day boundary discontinuities show the same pattern: the box-wing models perform better than the ECOM-only models and BW-1 performs better than BW-2. For comparison purposes, the quality measures are also given for orbits and clocks of Block IIR/IIR-M and Block IIF satellites computed with the box-wing models of Springer et al. (2014). The BW-1 model for the GPS III satellite is in general within the margin of the performance of the other satellite blocks although being close to the upper bound. For the clock residual STD, the ECOM-1, BW-1, and BW-2 solutions of GPS-74 outperform the older generations of GPS satellites. The stability of the GPS-74 clock will be discussed in detail in Section 6.

Overall, the three orbit-related performance metrics as well as the study of empirical SRP parameters provide strong support for use of the BW-1 a priori model in GPS-74 orbit determination. The BW-2 model, on the other hand, differs from BW-1 in the magnitude and phase of radial orbit perturbations and can thus provide clock offset estimates that are essentially free of 1/rev variations. However, the BW-2 model represents an almost cubic spacecraft body and is obviously incompatible with the actual GPS-74 geometry. Variation-of-parameter studies show that it is not possible to simultaneously remove the β-angle dependence of the estimated D_0 values and the orbit-periodic clock variations in a standard box-wing model using modified surface properties.

A proper explanation for the apparent discrepancy of GPS-74 SRP and clock analyses is presently missing. While thermally-induced clock variations might be considered to understand the conflicting results, it appears unlikely that

Please cite this article as: P. Steigenberger, S. Thoelert and O. Montenbruck, GPS III Vespucci: Results of half a year in orbit, Advances in Space Research, https://doi.org/10.1016/j.asr.2020.03.026

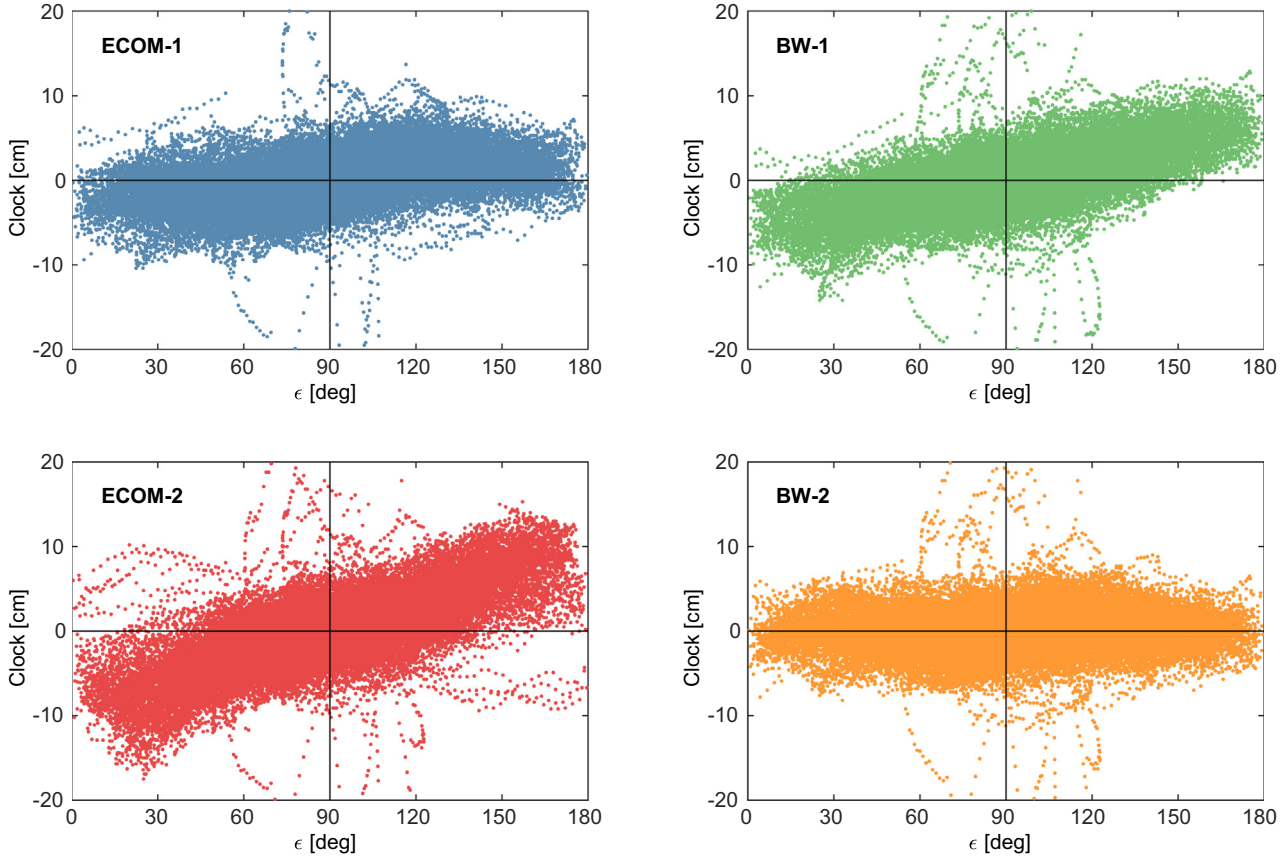

Fig. 7. GPS-74 clock residuals versus Earth-satellite-Sun angle ϵ for solutions with different SRP modeling.

Table 5
Orbit validation of different solar radiation pressure modeling approaches. The columns *IIR/IIR-M* and *IIF* denote the ranges of values for Block IIR/IIR-M and Block IIF satellites, respectively. The Block IIF satellites with Caesium clocks (GPS-65 and GPS-72) were excluded for the clock residual STD.

	ECOM-1	ECOM-2	BW-1	BW-2	IIR/IIR-M	IIF
Clock residual STD [cm]	3.1	4.5	3.7	2.8	5.3–12.1	4.2–8.9
Median 2-day orbit fit RMS [cm]	1.7	1.7	1.4	1.6	1.1–1.6	1.2–1.5
Median 1-day orbit prediction [cm]	15.8	14.8	13.5	14.6	8.6–17.3	9.7–17.1
Median day boundary discontinuities [cm]	5.8	5.3	4.2	5.1	3.2–4.4	3.1–4.1

such variations would be strictly in phase with the orbit angle as indicated by Fig. 7. Instead, a phase delay as found in the analysis of IIF observations would be expected (Montenbruck et al., 2012). On the other hand, the lack of laser retro reflectors on GPS-74 does not allow to study the possible presence of radial orbit errors as a source of periodic variations in the estimated clock offsets. In case the clock variations would indeed be related to deficiencies of the SRP model, refined ray-tracing models taking into account the detailed spacecraft structure along with shading effects appear as a promising way forward to further improve GPS III orbit and clock determination.

6. Clock stability

To characterize the stability of the GPS III RAFS, two different approaches are used: the one-way carrier phase (OWCP) method (Gonzalez and Waller, 2007) for analyzing the short term stability and a dedicated 30 s clock solution that was computed for selected days in addition to the 5 min clock solution. The OWCP approach is based on 1 Hz carrier phase observations of a GNSS station connected to a highly stable hydrogen maser. After subtracting the modeled range variation from the observed carrier phase, the combined drift of the hydrogen maser and the satellite clock is removed by a 1st order polynomial. By limiting the OWCP analysis to 10 min analysis intervals with high elevations of the selected satellites, tropospheric and ionospheric delays can be assumed to be constant and are also removed by the polynomial detrending. Single-frequency L5 observations for GPS and E5 AltBOC observations for Galileo are used as these observables have the lowest noise.

Allan deviations (ADEV) obtained from the OWCP of the IGS station MGUE00ARG (Malargue, Argentina) for the GPS III satellite GPS-74 (PRN G04), the GPS

Please cite this article as: P. Steigenberger, S. Thoelert and O. Montenbruck, GPS III Vespucci: Results of half a year in orbit, Advances in Space Research, https://doi.org/10.1016/j.asr.2020.03.026

Block IIF satellite GPS-68 (PRN G09, same orbital plane as GPS-74), and the Galileo FOC satellite GAL-219 (PRN E36) are shown in the left part of Fig. 8 covering integration times between 1 and 200 s. Whereas the GPS satellites are equipped with different generations of RAFSs, all Galileo satellites carry passive hydrogen masers (PHMs). For integration times up to 10 s, GPS-74 and GAL-219 have an almost identical ADEV behavior. As a separation between phase measurement noise and clock instability is not possible in the OWCP analysis, this curve provides an upper bound for the clock stability of these two satellites. The OWCP-derived ADEV of GPS-68 is about 50 to 100% higher than that of GPS-74 at these integration times. In view of a similar L5 phase measurement noise (Thoelert et al., 2019), this result suggests a notably improved short term stability of the GPS III RAFS compared to the earlier generation of Block IIF clocks.

ADEVs obtained from the 30 s clock solutions are given in the right part of Fig. 8 covering integration times between 30 and 36 000 s. At these integration times, the stability of the Block IIF and Block III clocks is almost identical. However, it has to be noted that a day with high β-angle has been chosen. For lower β-angles (thin lines in Fig. 8), a pronounced bump in the ADEV is present for Block IIF satellites at 10 000 s due to line bias variations, which degrade the performance of the apparent clock (Montenbruck et al., 2012). The Block III clock is not affected by line bias variations and does not show a dependence of the ADEV on the β-angle. Overall, the Galileo PHM shows the highest stability and reaches an ADEV of 10^{-14} at an integration time of 10 000 s.

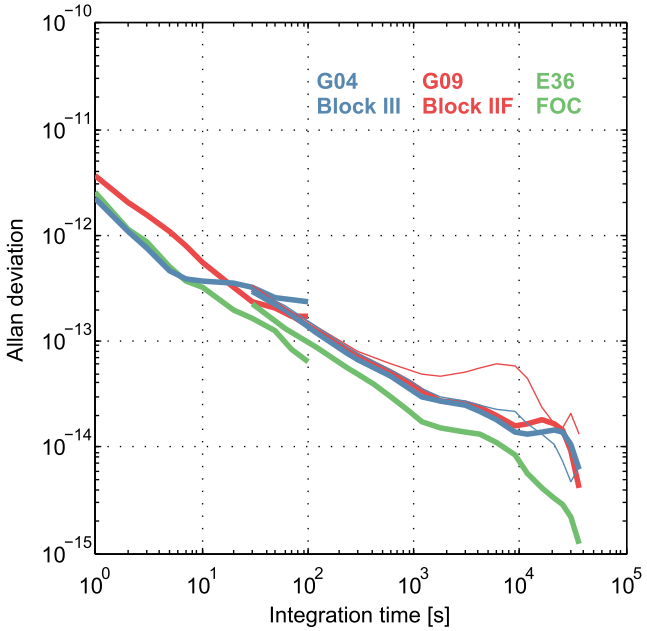

Fig. 8. Modified Allan deviation for GPS Block IIF (G09) and III (G04) Rubidium clocks as well as a Galileo FOC passive hydrogen maser (E36) for day of year 190/2019 (high β-angle). The lines covering 1 to 200 s originate from a one-way carrier phase analysis of the IGS station MGUE00ARG, the lines from 30 to 36 000 s from an orbit and clock determination with ECOM-1 SRP model and 30 s observation sampling. The thin lines for G09 and G04 refer to day of year 94/2019 (β-angle close to zero) and illustrate the impact of thermal clock variations with 2/rev periodicity in the IIF satellites. (For interpretation of the references to colour in this figure legend, the reader is referred to the web version of this article.)

7. Satellite antenna phase center offsets

Satellite antenna phase center offsets (PCOs) describe the vector between the center of mass of the satellite and the mean antenna phase center of the transmit antenna. In the IGS antenna model (currently igs14.atx, Rebischung and Schmid, 2016), estimated PCOs for the ionosphere-free linear combination of L1 and L2 are included for previous generations of GPS satellites. For Galileo and QZSS, frequency-specific calibrations provided by the system operators are included. GPS-74 is the first GPS satellite with antenna calibrations provided by the manufacturer. Frequency-specific PCOs for L1, L2, and L5 are published in Lockheed Martin (2019b) and listed in the left part of Table 6.

To verify these calibration values, PCOs were estimated from the ionosphere-free linear combination of L1 and L2 observations. The PCOs of all GPS satellites except for GPS-74 were fixed to igs14.atx and the GPS-74 PCOs were freely estimated together with the other parameters listed in Table 2. The resulting horizontal and vertical PCOs are shown in Fig. 9. Steigenberger et al. (2016) already demonstrated the dependence of the x- and y-offset estimates on the elevation of the Sun above the orbital plane due to correlations between these PCOs, the along-track direction of the orbit, and the SRP parameter D_0. Therefore, horizontal PCO estimates with formal errors exceeding 5 cm have been excluded (17% for x, 34% for y). The STD of the remaining estimates is on the 1 to 2 cm level. The weighted mean values of the estimated PCOs are given in the right column of Table 6. Whereas the mean y-offset differs from the manufacturer value by only 2 mm, a 3 cm difference occurs for the x-offset. However, this difference is still below the threefold mean formal error of the x-offset estimates of 3.8 cm. For the time series of z-offsets shown in the right plot of Fig. 9, it was not necessary to remove outliers. The STD of the z-offsets is about 5 cm and the mean value almost perfectly matches the manufacturer value with a difference of only 2 mm.

Table 6
Satellite antenna phase center offsets given in Lockheed Martin (2019b) converted to meters and to the IGS axes convention. L1/L2 denotes the ionosphere-free linear combination of L1 and L2.

	L1	L2	L5	L1/L2	Estimation
X [m]	−0.0181	−0.0162	−0.0163	−0.0210	-0.052 ± 0.027
Y [m]	0.0038	0.0031	0.0032	0.0048	0.007 ± 0.021
Z [m]	1.2324	0.7405	0.7787	1.9929	1.995 ± 0.046

Please cite this article as: P. Steigenberger, S. Thoelert and O. Montenbruck, GPS III Vespucci: Results of half a year in orbit, Advances in Space Research, https://doi.org/10.1016/j.asr.2020.03.026

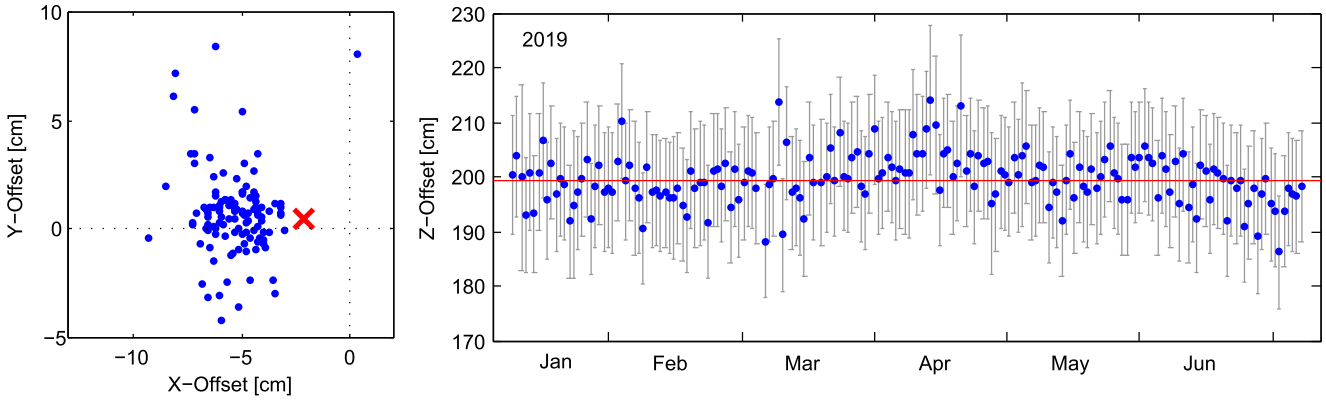

Fig. 9. Scatter plot of horizontal and time series of vertical estimated satellite antenna offsets of GPS-74. The error bars in the right plot represent the threefold formal errors. The red cross and the red line indicate the manufacturer value for the ionosphere-free linear combination of L1 and L2 in the IGS frame. (For interpretation of the references to colour in this figure legend, the reader is referred to the web version of this article.)

8. Outlook

Shortly after its launch, the first GPS III spacecraft started transmitting unhealthy navigation signals for about half a year with PRN code G04. During this time period, a 2 months long-term propagation test of the broadcast ephemerides was performed resulting in range errors of up to 600 m. Spacecraft geometry obtained from a scale model and default optical properties provided the basis for developing a box-wing model for GPS-74. This BW-1 model performs slightly better than the empirical ECOM models. However, periodic errors in the estimated satellite clock parameters with an amplitude of about 10 cm are a side effect of BW-1. These errors could be removed by altering the box surfaces to an almost cubic satellite body that does not represent the true dimensions of the stretched shape of the GPS III spacecraft at all. In contrast to the also stretched but much lighter Galileo satellites, ECOM-1 performs quite well for GPS-74, even better than ECOM-2. The question why models developed for cubic satellites, namely ECOM-1 and the BW-2 model, reduce systematic effects in the clock residuals of the cuboid GPS III spacecraft remains a topic for future research. However, more detailed information on the satellite geometry, shading of parts of the satellite body as well as optical properties are a prerequisite for refined SRP modeling.

The second GPS III satellite named Magellan was launched on August 22, 2019. Two launches per year are planned for the time period 2019–2022 and the last GPS III satellite is expected to be launched in 2023. A contract for 22 GPS III Follow-on (IIIF) satellites was awarded to Lockheed Martin in September 2018 (Cameron, 2019). These satellites will provide a redesigned nuclear detonation detection system, a laser retro-reflector array for satellite laser ranging, a search and rescue payload, and a regional military protection capability providing up to −140 dBW signal power for the M-code (Zinn, 2016). The latter requires an additional dish antenna that will pose a major challenge for SRP modeling. A full constellation of 32 GPS III and IIIF satellites is expected by 2034 (Whitney, 2017).

Acknowledgments

The International GNSS Service (IGS) is acknowledged for providing GPS observation data.

References

Alexander, K., Martin III, H.W., 2018. GPS program update. Presentation at 13th Meeting of the International Committee on Global Navigation Satellite Systems, Xi'an, China. URL http://www.unoosa.org/documents/pdf/icg/2018/icg13/02.pdf.

Arnold, D., Meindl, M., Beutler, G., Dach, R., Schaer, S., Lutz, S., Prange, L., Sosnica, K., Mervart, L., Jäggi, A., 2015. CODE's new solar radiation pressure model for GNSS orbit determination. J. Geod. 89 (8), 775–791. https://doi.org/10.1007/s00190-015-0814-4.

Betz, J., Blanco, M., Cahn, C., Dafesh, P., Hegarty, C., Hudnut, K., Kasemsri, V., Keegan, R., Kovach, K., Lenahan, L., Ma, H., Rushanan, J., Sklar, D., Stansell, T., Wang, C., Yi, S., 2007. Enhancing the future of civil GPS: overview of the L1C signal. Inside GNSS 2 (3), 42–49.

Beutler, G., Brockmann, E., Gurtner, W., Hugentobler, U., Mervart, L., Rothacher, M., Verdun, A., 1994. Extended orbit modeling techniques at the CODE processing center of the international GPS service for geodynamics (IGS): theory and initial results. Manuscr. Geod. 19, 367–386.

Bhattarai, S., Ziebart, M., Allgeier, S., Grey, S., Springer, T., Harrison, D., Li, Z., 2019. Demonstrating developments in high-fidelity analytical radiation force modelling methods for spacecraft with a new model for GPS IIR/IIR-M. J. Geod. 93 (9), 1515–1528. https://doi.org/10.1007/s00190-019-01265-7.

Boehm, J., Heinkelmann, R., Schuh, H., 2007. Short note: a global model of pressure and temperature for geodetic applications. J. Geod. 81 (10), 679–683. https://doi.org/10.1007/s00190-007-0135-3.

Boehm, J., Niell, A., Tregoning, P., Schuh, H., 2006. Global Mapping Function (GMF): a new empirical mapping function based on numerical weather model data. Geophys. Res. Lett. 33 (7). https://doi.org/10.1029/2005GL025546, L07304.

Bury, G., Zajdel, R., Sośnica, K., 2019. Accounting for perturbing forces acting on Galileo using a box-wing model. GPS Solut. 23 (74). https://doi.org/10.1007/s10291-019-0860-0.

Cabinet Office, 2019. QZSS satellite information. URL https://qzss.go.jp/en/technical/qzssinfo/index.html

Please cite this article as: P. Steigenberger, S. Thoelert and O. Montenbruck, GPS III Vespucci: Results of half a year in orbit, Advances in Space Research, https://doi.org/10.1016/j.asr.2020.03.026

Cameron, A., 2019. That was then. This is now. GPS World 30 (3), 18–30.
Cozzens, T., 2019. Second GPS III in orbit, responding to commands. URL https://www.gpsworld.com/second-gps-iii-in-orbit-responding-to-commands/.
Darugna, F., Steigenberger, P., Montenbruck, O., Casotto, S., 2018. Ray-tracing solar radiation pressure modeling for QZS-1. Adv. Space Res. 62 (4), 935–943. https://doi.org/10.1016/j.asr.2018.05.036.
Dilssner, F., 2010. GPS IIF-1 satellite: antenna phase center and attitude modeling. Inside GNSS 5 (6), 59–64.
Duan, B., Hugentobler, U., Selmke, I., 2019. The adjusted optical properties for Galileo/BeiDou-2/QZS-1 satellites and initial results on BeiDou-3e and QZS-2 satellites. Adv. Space Res. 63 (5), 1803–1812. https://doi.org/10.1016/j.asr.2018.11.007.
Erwin, S., 2019. Air Force to upgrade existing GPS ground control system while next-generation OCX lags. Space News, https://spacenews.com/air-force-to-upgrade-existing-gps-ground-control-system-while-next-generation-ocx-lags/.
Fliegel, H.F., Gallini, T.E., 1996. Solar force modeling of Block IIR Global Positioning System satellites. J. Spacecraft Rockets 33 (6), 863–866. https://doi.org/10.2514/3.26851.
Gonzalez, F., Waller, P., 2007. One-way carrier phase. In: Frequency Control Symposium, 2007 Joint with the 21st European Frequency and Time Forum. pp. 517–522.
GPS World, 2019. Ground system COps connects with orbiting GPS III satellite. GPS World. URL https://www.gpsworld.com/ground-system-cops-connects-with-orbiting-gps-iii-satellite/.
GSA, 2017. Galileo satellite metadata. https://www.gsc-europa.eu/support-to-developers/galileo-satellite-metadata.
Hegarty, C., 2017. The Global Positioning System (GPS). In: Teunissen, P., Montenbruck, O. (Eds.), Springer Handbook of Global Navigation Satellite Systems. Springer, Cham, Switzerland, pp. 197–218 (Chapter 7). https://doi.org/10.1007/978-3-319-42928-1_7.
IS-GPS-200K, 2019. Interface specification IS-GPS-200: Navstar GPS Space Segment/Navigation User Segment Interfaces. Tech. rep., Global Positioning Systems Directorate Systems Engineering & Integration. URL https://www.gps.gov/technical/icwg/IS-GPS-200K.pdf.
IS-GPS-800F, 2019. Navstar GPS Space Segment/User Segment L1C interface. Tech. rep., Global Positioning System Directorate Systems Engineering & Integration. URL http://www.gps.gov/technical/icwg/IS-GPS-800F.pdf.
Johnston, G., Riddell, A., Hausler, G., 2017. The International GNSS Service. In: Teunissen, P., Montenbruck, O. (Eds.), Springer Handbook of Global Navigation Satellite Systems. Springer, Cham, Switzerland, pp. 967–982. https://doi.org/10.1007/978-3-319-42928-1_33 (Chapter 33).
Kouba, J., 2009. A simplified yaw-attitude model for eclipsing GPS satellites. GPS Solut. 13 (1), 1–12. https://doi.org/10.1007/s10291-008-0092-1.
Li, Z., Ziebart, M., Bhattarai, S., Harrison, D., Grey, S., 2018. Fast solar radiation pressure modelling with ray tracing and multiple reflections. Adv. Space Res. 61 (9), 2352–2365. https://doi.org/10.1016/j.asr.2018.02.019.
Lockheed Martin, 2019a. Lockheed Martin's second GPS III satellite is encapsulated prior to launch. URL https://www.flickr.com/photos/lockheedmartin/48233129441/in/album-72157625171465765/.
Lockheed Martin, 2019b. SVN74 APC & ISC data release, January 2019.
Marquis, W., Shaw, M., 2011. Design of the GPS III space vehicle. ION ITM 2011, 3067–3075.
Melbourne, W.G., 1985. The case for ranging in GPS based geodetic systems. In: Goad, C. (Ed.), Proceedings of the First International Symposium on Precise Positioning with the Global Positioning System. U.S. Department of Commerce, Rockville, Maryland, pp. 373–386.
Montenbruck, O., Hugentobler, U., Dach, R., Steigenberger, P., Hauschild, A., 2012. Apparent clock variations of the Block IIF-1 (SVN62) GPS satellite. GPS Solut. 16 (3), 303–313. https://doi.org/10.1007/s10291-011-0232-x.
Montenbruck, O., Schmid, R., Mercier, F., Steigenberger, P., Noll, C., Fatkulin, R., Kogure, S., Ganeshan, A., 2015a. GNSS satellite geometry and attitude models. Adv. Space Res. 56 (6), 1015–1029. https://doi.org/10.1016/j.asr.2015.06.019.
Montenbruck, O., Steigenberger, P., Darugna, F., 2017. Semi-analytical solar radiation pressure modeling for QZS-1 orbit-normal and yaw-steering attitude. Adv. Space Res. 59 (8), 2088–2100. https://doi.org/10.1016/j.asr.2017.01.036.
Montenbruck, O., Steigenberger, P., Hauschild, A., 2015b. Broadcast versus precise ephemerides: a multi-GNSS perspective. GPS Solut. 19 (2), 321–333. https://doi.org/10.1007/s10291-014-0390-8.
Montenbruck, O., Steigenberger, P., Hugentobler, U., 2015c. Enhanced solar radiation pressure modeling for Galileo satellites. J. Geod. 89 (3), 283–297. https://doi.org/10.1007/s00190-014-0774-0.
Prange, L., Orliac, E., Dach, R., Arnold, D., Beutler, G., Schaer, S., Jäggi, A., 2017. CODE's five-system orbit and clock solution – the challenges of multi-GNSS data analyis. J. Geod. 91 (4), 345–360. https://doi.org/10.1007/s00190-016-0968-8.
Rebischung, P., Schmid, R., 2016. IGS14/igs14.atx: a new framework for the IGS products. Poster at AGU Fall Meeting, San Francisco, USA, G41A-0998. URL https://mediatum.ub.tum.de/doc/1341338/file.pdf.
Rodriguez Solano, C.J., 2014. Impact of non-conservative force modeling on GNSS satellite orbits and global solutions. Ph.D. thesis. Technische Universität München. URL http://nbn-resolving.de/urn/resolver.pl?urn:nbn:de:bvb:91-diss-20140822-1188612-0-8.
Rodriguez-Solano, C.J., Hugentobler, U., Steigenberger, P., 2012. Adjustable box-wing model for solar radiation pressure impacting GPS satellites. Adv. Space Res. 49 (7), 1113–1128. https://doi.org/10.1016/j. asr.2012.01.016.
Saastamoinen, J., 1972. The Use of Artifical Satellites for Geodesy. Vol. 15 of Geophysical Monograph Series. American Geophysical Union, Ch. Atmospheric Correction for the Troposphere and Stratosphere in Radio Ranging Satellites, pp. 247–251. http://dx.doi.org/10.1029/GM015p0247.
Sibthorpe, A., Bertiger, W., Desai, S.D., Haines, B., Harvey, N., Weiss, J. P., 2011. An evaluation of solar radiation pressure strategies for the GPS constellation. J. Geod. 85 (8), 505–517. https://doi.org/10.1007/s00190-011-0450-6.
Sosnica, K., Thaller, D., Dach, R., Steigenberger, P., Beutler, G., Arnold, D., Jäggi, A., 2015. Satellite laser ranging to GPS and GLONASS. J. Geod. 89 (7), 725–743. https://doi.org/10.1007/s00190-015- 0810-8.
Springer, T., 2009. NAPEOS mathematical models and algorithms. Tech. Rep. DOPS-SYS-TN-0100-OPS-GN, ESA/ESOC, Darmstadt.
Springer, T., Otten, M., Flohrer, C., Pereira, F., Gini, F., Enderle, W., 2014. GNSS satellite orbit modeling at ESOC. Poster at IGS Workshop 2014, Pasadena, USA. http://www.igs.org/assets/pdf/Workshop%202014%20-%20PS10%20-%20Springer%20-%202163%20-%20GNSS%20Satellite%20Orbit%20Modeling%20at%20ESOC.pdf.
Steigenberger, P., Fritsche, M., Dach, R., Schmid, R., Montenbruck, O., Uhlemann, M., Prange, L., 2016. Estimation of satellite antenna phase center offsets for Galileo. J. Geod. 90 (8), 773–785. https://doi.org/10.1007/s00190-016-0909-6.
Steigenberger, P., Hugentobler, U., Loyer, S., Perosanz, F., Prange, L., Dach, R., Uhlemann, M., Gendt, G., Montenbruck, O., 2015. Galileo orbit and clock quality of the IGS Multi-GNSS Experiment. Adv. Space Res. 55 (1), 269–281. https://doi.org/10.1016/j.asr.2014.06. 030.
Steigenberger, P., Thoelert, S., Montenbruck, O., 2018. GNSS satellite transmit power and its impact on orbit determination. J. Geod. 92 (6), 609–624. https://doi.org/10.1007/s00190-017-1082-2.
Steigenberger, P., Thoelert, S., Montenbruck, O., 2019. GPS and GLONASS satellite transmit power: Update for igs repro3. TN 19-01. DLR/GSOC. URL http://acc.igs.org/repro3/TX_Power_20190711.pdf.
Thoelert, S., Steigenberger, P., Montenbruck, O., Meurer, M., 2019. Signal analysis of the first GPS III satellite. GPS Solut. 23 (92). https://doi.org/10.1007/s10291-019-0882-7.

Please cite this article as: P. Steigenberger, S. Thoelert and O. Montenbruck, GPS III Vespucci: Results of half a year in orbit, Advances in Space Research, https://doi.org/10.1016/j.asr.2020.03.026

U.S. Air Force, 2015. Global Positioning System. URL https://www.af.mil/About-Us/Fact-Sheets/Display/Article/104610/global-positioning-system/.

Wübbena, G., 1985. Software developments for geodetic positioning with GPS using TI-4100 code and carrier measurements. In: Goad, C. (Ed.), Proceedings of the First International Symposium on Precise Positioning with the Global Positioning System. U.S. Department of Commerce, Rockville, Maryland, pp. 403–412.

Whitney, S., 2017. GPS status & modernization progress: Service, satellites, control segment, and military GPS user equipment. In: ION GNSS+ 2017. pp. 826–842.

Wielicki, B.A., Barkstrom, B.R., Harrison, E.F., Lee, R.B., Smith, G.L., Cooper, J.E., 1996. Clouds and the Earth's Radiant Energy System (CERES): an Earth observing system experiment. Bull. Am. Meteorol. Soc. 77 (5), 853–868. https://doi.org/10.1175/1520-0477(1996)077<0853:CATERE>2.0.CO;2.

Wu, A., Feess, B., 2000. Development and evaluation of GPS space clocks for GPS III and beyond. In: 32nd Annual Precise Time and Time Interval (PTTI) Meeting. pp. 389–399.

Zhao, Q., Chen, G., Guo, J., Liu, J., Liu, X., 2018. An a priori solar radiation pressure model for the QZSS Michibiki satellite. J. Geod. 92 (2), 109–121. https://doi.org/10.1007/s00190-017-1048-4.

Zinn, A., 2016. GPS status & modernization progress: Service, satellites, control segment, and military GPS user equipment. Presentation at 17th Meeting of the National Space-Based Positioning, Navigation, and Timing Advisory Board, National Harbor, Maryland, USA. https://www.gps.gov/governance/advisory/meetings/2016-05/zinn.pdf.

Please cite this article as: P. Steigenberger, S. Thoelert and O. Montenbruck, GPS III Vespucci: Results of half a year in orbit, Advances in Space Research, https://doi.org/10.1016/j.asr.2020.03.026